First publ. in: Physical Chemistry Chemical Physics 12 (2010), 38, pp. 11984-11992, DOI: 10.1039/C0CP00819B

$BaCO_3$ mesocrystals: new morphologies using peptide–polymer conjugates as crystallization modifiers†

Tongxin Wang,[ab] James Mitchell,[b] Hans Börner,‡[a] Helmut Cölfen§*[a] and Markus Antonietti*[a]

DOI: 10.1039/c0cp00819b

Nanocrystal superstructures of barium carbonate ($BaCO_3$) which exhibit unusual morphologies are obtained by the carbon dioxide vapor diffusion technique in the presence of poly(ethylene oxide)-*block*-eicosa aspartate (PEO-*b*-Asp_{20}). The highly effective bioconjugate acts as a crystal growth modifier over a broad range of concentrations. Instead of commonly observed branched needles, the morphology can be systematically varied along different twinned growth patterns towards well-defined branched dumbbells. Detailed analysis of the crystal substructures with high resolution scanning electron microscopy (HRSEM) and dynamic light scattering (DLS) discloses a potential growth mechanism of the superstructures and reveals the role of the polymeric bioconjugate therein.

Introduction

The controlled growth of crystal superstructures with defined features *e.g.* hierarchical organization, spatial orientation, porosity, distinct functional and mechanical interfaces from the nanometre toward the micrometre scale is of interest to realize modern strategies of nanoscience and nanochemistry.[1,2] Besides, fundamental understanding of the formation processes of crystals or inorganic–organic hybrids affects also many practical applications. As nucleation and growth are delicately balanced, sensitive processes, crystallization can be conveniently modified by the addition of nucleation agents, crystal or crystal-precursor stabilizers.[2] During recent decades it became established that in general ternary components like for instance a broad choice of (co)solvents,[3] low molecular additives, surfactants and functional polymers affect crystallization processes (for recent reviews, *cf.* to the following ref. 4–17).

In addition to classical nucleation and growth control, also non-classical pathways of crystallization have been identified.[5,9,18–21] These routes proceed *via* colloidal intermediates, directed assembly of nano-scaled building blocks and mesoscale transformation.[5,9,18–21] In the case of a non-classical crystallization process, crystalline structures are not constructed by the addition of single ions onto nucleated crystals, but instead by the assembly and/or transformation of larger tectonic units. Mesoscale assembly and transformation was reported not only to take place for inorganic crystalline solids such as iron oxides,[22] cerium oxide,[23] copper oxalates,[6] copper oxides,[24] or barium sulfates,[25] but also for crystalline organic systems like D,L-alanine[26] and biominerals.[27,28] There are many more examples, which are summarized in recent overviews.[9,18–21]

The role of polymer additives within those directed mesoscale assembly processes is manifold, and often multiple functions can be dedicated to the additives as discussed in detail in previous contributions.[29–32] For instance, polymer additives like double hydrophilic block copolymers[33] bind ions by electrostatic counter ion condensation. On the one hand this down regulates (blocks) the classical ionic growth path. On the other hand, a suitable template is provided that influences the geometry of the crystal nuclei and thus sets the stage for crystal shape control at a rather early phase. It should be noted that a similar multifunctional character can be found in biological molecules, suspected to take part in biological crystal control. Metastable intermediates, such as amorphous precursor structures, are colloidally stabilized by a surface layer of polymers. In the ongoing crystallization process, the polymer can alter the shape of the developing nanocrystals by selective adsorption and/or enrichment onto specific crystal faces. The adsorbed polymer additives are frequently dynamic enough to induce and guide the directed aggregation. Through a change of interaction potential[30] the assembly can be impressively directional and anisotropic.[34] Such a structure formation is clearly different to the classical crystallization process, which points back to early last century.[35]

The specific reasons for a vectorial alignment of mesoscopic building units with respect to each other as well as the possibility to obtain crystalline superstructures with architectures and geometries very different from the primary building blocks are currently explored.[29–32,35,36] In a recent study, a peptide–polymer conjugate has been introduced as a well-defined model system, which exhibited a monodisperse peptide segment as functional block. The poly(ethylene oxide)-*block*-eicosa aspartate (PEO-*b*-Asp_{20}) assures a sharply defined structure–property relationship due to the absence of chemical- and

[a] *Max-Planck-Institute of Colloids and Interfaces, Department of Colloid Chemistry, Research Campus Golm, D-14424 Potsdam, Germany*
[b] *Crest Center for Nanomaterials, Howard University, Washington, DC 20059, USA*

† Electronic supplementary information (ESI) available: Surface cut of (110) and (001) faces of witherite and polarized image of the dumbell structure. See DOI: 10.1039/c0cp00819b

‡ Present address: Department of Chemistry, Humboldt-Universität zu Berlin, Brook Taylor-Str. 2, Berlin, Germany. pape@mpikg.mpg.de
§ Present address: University of Konstanz, Physical Chemistry, Universitätsstr. 10, D-78457 Konstanz, Germany. helmut.coelfen@uni-konstanz.de

molecular weight distributions in the functional Asp_{20} segment. The additive proved to act as a very effective double hydrophilic block copolymer that showed the onset of modification activity already at concentrations of 1 ppm.[31] The low concentration of additive molecules required suggests a high dynamics within the crystal–additive interactions and excludes somehow the naive pictures of static additives that block distinct crystal surfaces to gain structural control of crystal growth.

It is the focus of the present contribution to extend these primary observations on PEO-*b*-Asp_{20} controlled calcite mesocrystals to a related mineral system, barium carbonate. $BaCO_3$ crystallizes dominantly in the witherite polymorph and thus constitutes an ideal candidate to investigate the variation of the meso-morphology over a broad range of PEO-*b*-Asp_{20} concentration without being concerned by a transition of crystal polymorph. We hope to provide additional evidence to understand how and at which step the polymer interferes with the crystallization process and how mesostructure alignment can be well controlled.

Experimental

Instrumentation

Optical microscopy in solution and scanning electron microscopy (SEM) were applied to all samples. The SEM measurements were performed on a LEO 1550 GEMINI instrument. Optical microscopy images were taken for samples in solution with an Olympus BX50 or BX41 microscope connected to a MONACOR TVCCD-460 colour camera. Light scattering was conducted on a Malvern zeta nano-sizer. The surface cleavage of the crystal faces, the unit cell structure, and the modeling of morphologies were performed with the *Cerius*[2] and *Materials Studio 4.3* software (Accelrys).

Materials

The following chemicals were purchased from the indicated suppliers and were used without further purification: $BaCl_2 \cdot 2H_2O$ (Fluka, $\geq$ 99%), $(NH_4)_2CO_3$ (Fluka). Fmoc Asp(*t*Bu) OH, *N*-methyl-2-pyrrolidone (NMP, peptide grade), and 2-(1*H*-benzotriazol-1-yl)-1,1,3,3-tetramethyluronium hexafluorophosphate (HBTU) were received from IRIS Biotech, Germany. Double distilled water was used for the preparation of the crystallization solutions.

Bioconjugate synthesis

The PEO-*b*-Asp_{20} conjugate was synthesized by an inverse conjugation route, following standard FastMoc protocols (double coupling) for solid-phase supported peptide synthesis (SPPS).[37] PEO pre-loaded polystyrene resin (0.24 mmol g^{-1}; $M_{n,PEO}$ = 3200 g mol^{-1}, M_w/M_n = 1.06) was applied.[38] The peptide segment was assembled by sequential addition of Fmoc Asp(*t*Bu) OH amino acid derivative on an ABI433A peptide synthesizer.[39] The SPPS was performed in NMP, and HBTU facilitated the formation of the amide bond.[38] After liberation of the conjugate from the support, the fully deprotected conjugate was isolated by precipitation in diethyl ether and purified by dialysis against Millipore water (MWCO 3000) to obtain the conjugate in 62% yield. ^1H NMR spectroscopy confirmed the chemical structure of the conjugate: δ = 2.84 (br m, ~40 H, βCH_2, Asp), 3.69 (br m, 280 H, CH_2CH_2 (PEO)), 4.76 (br m, 20 H, αCH, Asp) ppm.

Crystallization

The mineralization was performed by using a CO_2 gas diffusion setup as described by Addadi and coworkers.[40] All glassware including glass bottles and small pieces of glass substrates were cleaned as follows: firstly sonicated in ethanol, then rinsed with distilled water, further soaked with a H_2O–HNO_3 (65%)–H_2O_2 (1 : 1 : 1, v/v/v) solution, then rinsed with doubly distilled H_2O, and finally dried at room temperature. Crystallization was performed in a closed desiccator at room temperature with the concentrations of the $BaCl_2$ and PEO-*b*-Asp_{20} conjugate as the independent variables (Table 1). The crystallization mixture was distributed equally into several glass bottles with a glass slide (1 mL volume per bottle). The bottles were sealed with Parafilm and punctured three times with a needle before placing the bottles into the desiccator (inner diameter 250 mm). Two glass vials filled with 2 g of freshly crushed ammonium carbonate were sealed with Parafilm, punched with three holes and placed at the bottom of the desiccator. Crystal growth kinetics was obtained by removing crystallization bottles from the desiccator at different times. Immediately after samples were taken, the solution was investigated by particle size measurement *via* light scattering. The glass slide with the crystals was rinsed with distilled water and examined by optical microscopy followed by SEM after drying at room temperature.

Results and discussion

With the presented crystallization set-up and procedure, free barium carbonate crystallization without polymer gives within 1 day highly intergrown, dendritic crystalline brushes of needles, depicted in Fig. 1. X-Ray diffraction analysis confirmed the presence of pure Witherite ($BaCO_3$) with cell constants a = 6.433, b = 5.315, c = 8.904 (orthorhombic structure; space group *Pnma*).

For the polymer controlled crystallization, a reasonable working window of Ba^{2+} concentrations between 2.5–10 mM and a polymer concentration window of 0.1 g L^{-1}–1 g L^{-1} were identified. The corresponding samples are summarized in Table 1.

Table 1 Sample code for crystals prepared from different concentrations of polymer and Ba^{2+}

	$[Ba^{2+}]$ = 10 mM	$[Ba^{2+}]$ = 5 mM	$[Ba^{2+}]$ = 2.5 mM
[Polymer] = 1.0 g L^{-1}	Aa	Ba	Ca
[Polymer] = 0.5 g L^{-1}	Ab	Bb	Cb
[Polymer] = 0.1 g L^{-1}	Ac	Bc	Cc

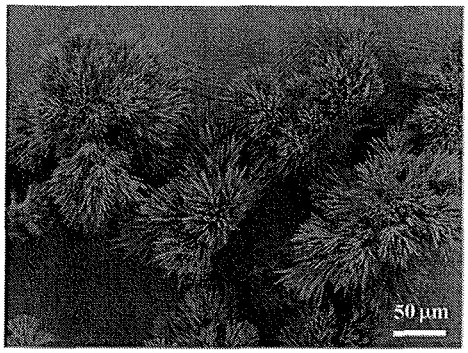

Fig. 1 Default crystals of witherite, crystallized at 10 mM Ba^{2+} concentration by the CO_2-gas diffusion method without additives.

For all polymer concentrations of 1.0 g L^{-1} and higher (samples Aa, Ba, Ca) or high relative polymer concentration (Bb and Cb), homogeneous nucleation of crystal structures was essentially blocked, and only heterogeneous growth from defects on the glass slides was found. The morphology of the resulting structures however is quite interesting, as depicted in Fig. 2. Crystals from the highest polymer concentration (1.0 g L^{-1}) show semi-spherical structure/spheres nucleated from the glass slides), no matter whether the Ba^{2+} concentration is 10 mM, 5 mM or 2.5 mM (Fig. 2: Aa, Ba, Ca). In comparison to that, all the crystals show dumbbell structures when the polymer concentration is lowest (0.1 g L^{-1}) (Fig. 2: Ac, Bc, Cc). This indicates that the polymer/Ba^{2+} ratio plays a key role in the morphological control. The crystal morphology is a result of the competitive effect between polymer modification and inorganic crystal growth of $BaCO_3$. A higher polymer/Ba^{2+} ratio leads to strong surface modification, and a close-to-spherical structure is formed. However, at lower polymer/Ba^{2+} ratio, less polymer leads to weaker modification, thus crystallization is dominated by the driving force of directional $BaCO_3$ growth. Most interesting is the development of crystal morphology for the intermediate polymer concentration (0.5 g L^{-1}, Fig. 2: Ab, Bb, Cb) which nicely confirms this hypothesis. In this case, the highest Ba^{2+} concentration (10 mM, Fig. 2: Ab) with the lowest polymer/Ba^{2+} ratio leads to a dumbbell structure while the other two lower Ba^{2+} concentration lead to spherical structures (Fig. 2: Bb, Cb).

At high polymer concentrations, the overall shape of the heteronucleated crystal superstructures is about semicircular with a diameter of 30–50 µm, with the outside of the superstructures being very rough and being composed of porous, inter-grown crystals (Fig. 3: Aa, Ba and Ca). We attribute the intracrystalline porosity, which is independent of Ba^{2+} concentration, to the remainders of included polymer additives, as it was reported for latex particles and ZnO[41] or for pores in $CaCO_3$ templated by micelles.[42] The crystal growth seems to occur along the tips of the subcrystals, thus preserving the roughness and high surface area of the structures throughout crystal growth. It is obvious that such a structure does not comply with simple pictures of surface area minimization or Ostwald ripening. Interestingly, the surface structure is getting finer and more differentiated (or the corresponding number of growth tips larger) when the relative amount of polymer is increased (Aa to Ca). This will be discussed in context of the other experiments below.

For lower polymer concentrations, a morphology change is observed. Besides a few heterogeneously nucleated structures similar to those previously discussed, the majority of material is crystallizing homogeneously from solution

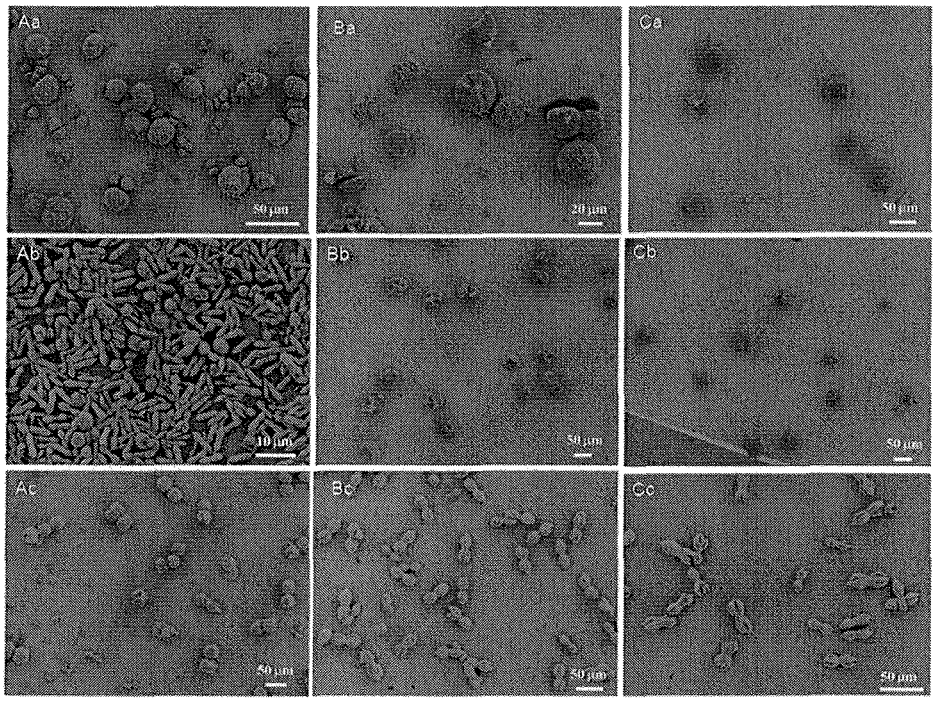

Fig. 2 Overview image of crystals obtained from different concentrations of polymer and Ba^{2+} listed in Table 1.

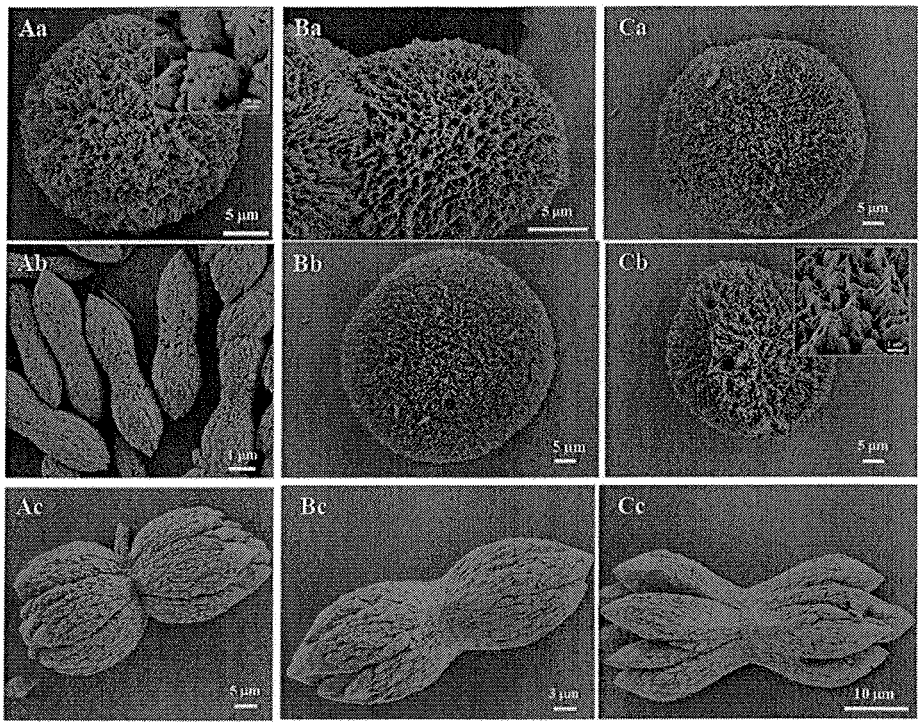

Fig. 3 Highly magnified images of crystals obtained from different concentrations of polymer and Ba^{2+} listed in Table 1. The inset higher magnified images of the surface characteristics indicate the surface roughness, nano-scale subunits and porosity.

towards a very special elongated morphology. This is exemplarily shown for sample Ab (addition of 0.5 g L^{-1} of PEO-*b*-Asp_{20} to a 10 mM Ba^{2+} solution) in Fig. 3: Ab. These crystals are composed of nanoparticles, and selected area electron diffraction (SAED) shows an oriented spot pattern which is characteristic for mesocrystals (Fig. 4). It is well possible that the SAED in Fig. 4 does not correspond to that of a single $BaCO_3$ crystal due to microtoming artifacts of the brittle embedded mesocrystals, but the spot like pattern even without arcs shows a very high mutual orientation of the nanoparticles in the mesocrystal shown in Fig. 4.

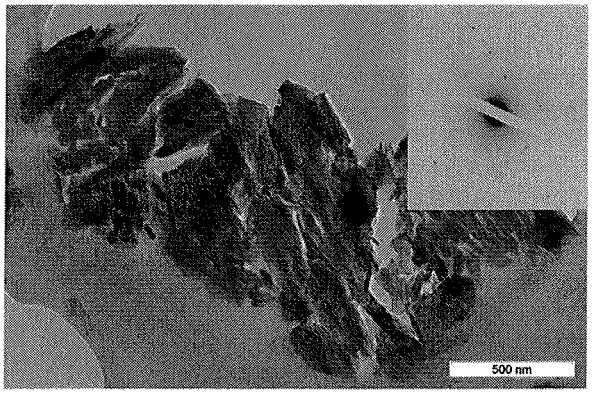

Fig. 4 TEM on a microtome cut of sample Ab, the brittle mesocrystal sample, and the corresponding SAED image of the TEM micrograph area showing a spot diffraction pattern.

The crystalline species Ab are much smaller than the spherical ones at higher polymer concentration and very homogeneous in morphology and size. This is due to the control provided by the polymer. The morphology has changed to peanut-like crystal superstructures with an overall length of about 10 μm and a cross-section of about 2.5 μm. The inner structure is remarkably different from the center to the tip of the structures: the constituting particles are smaller and ill-defined in the middle, and structural porosity and packing faults are clearly visible, whereas towards the tips the constituting primary crystals are getting larger and improve their mutual packing. The more disordered and smaller nanoparticles in the inner structure are also associated to a higher nanoparticle solubility as an alternative explanation for the observed defects.

The construction principle of the crystal superstructures is getting clearer when this sample is compared to the related structures made from 0.1 g L^{-1} polymer concentration and 10 mM, 5 mM and 2.5 mM Ba^{2+} solution (the C-series) (Fig. 3: Ac, Bc, and Cc). The peanut structures have grown to a much larger size under those conditions (overall length *ca.* 50–80 μm), which reflects the fact that less polymer allows for less stabilization of nanoparticle building units and therefore formation of a lower number of mesocrystals. Sample Ac has expressed a more complicated peanut like morphology discussed below, whereas for the two lower mineral concentrations, the mesoscale assemblies develop defined joint outer crystal faces. The superstructures are still twinned and grow in two opposite directions, but develop in the centre perpendicular to the growth direction either in a rectangular or a hexagonal

cross section. Rectangular and hexagonal cross-sections are co-occurring in both samples.

Each of the sides of the superstructure opens up to 7 branches, with one central and six side arms reflecting the hexagonal symmetry perpendicular to the growth direction. For sample Bc, the branches are still closed towards the overall peanut shape, whereas for sample Cc the lower mineral concentration allows the development of clearly separated branches, with an opening angle being constant throughout the sample of about 125°.

This branching is reminiscent to a similar growth pattern described by Kniep *et al.* for fluoroapatite in gelatin matrices,[43–46] where, however, some generations of branches were observed. Our $BaCO_3$ model system obviously stops at the first step and allows us to analyse the single branching step. Looking at the equilibrium morphology of the orthorhombic witherite, the construction principle of the mesocrystals can be qualitatively understood (Fig. 5) on the basis of classical crystallization of the nanoparticle subunits. It is important to note in this respect that the primary nanoparticles, which are needed to construct the mesocrystals, are nucleated *via* a classical crystallization and growth process and can therefore be modelled. The {110} family of four faces is polar and can be purely cationic or anionic (Fig. S1, ESI†). It is therefore a high energy face and according to Wulff's rule[35] a growth face. The same is true for the {001} faces, which are however not expressed in the morphology (Fig. S2, ESI†). These faces are adsorption faces for the negatively charged polymer block and thus get blocked from further growth making up the nanoparticle building units. The hexagonal cross section along the *c*-direction becomes expressed (Fig. 5c) and can explain the observed branching into 7 branches. From these considerations, the *c*-axis can be considered as the long axis of the dumbbell structures.

Besides the micron-sized mesocrystals shown in Fig. 2 and 3, we observe coexisting nanoparticles in solution by dynamic light scattering (DLS). The particle sizes from solution are dependent on either the concentration of polymer or Ba^{2+}, respectively (Fig. 6). Higher concentration of either polymer or Ba^{2+} leads to a larger nanoparticle size during crystallization. When the Ba^{2+} concentration is 10 mM, the particle sizes are 364, 553 and 692 nm, respectively, with increase of the polymer concentration (Fig. 6a). When the polymer concentration is 1 g L^{-1}, the highest Ba^{2+} concentration

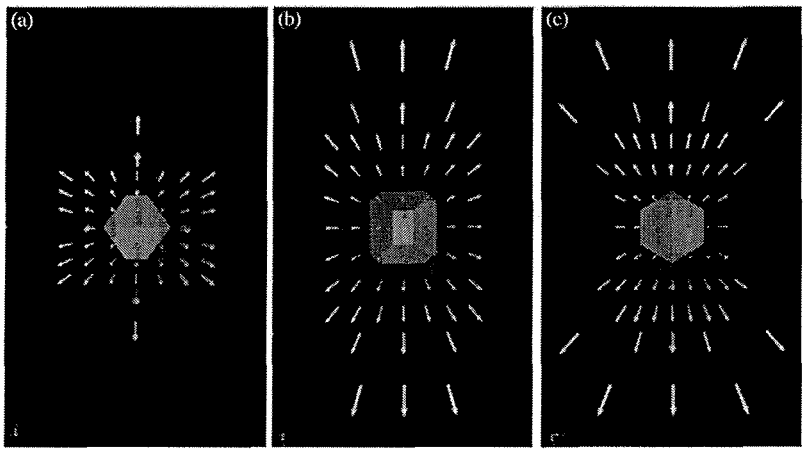

Fig. 5 Morphology calculation of witherite in vacuum with Materials Studio 4.3. (Accelrys). The growth velocities of the different faces are symbolized as arrows with the size/length of the arrows being proportional to the growth speed of the face. The crystal is viewed along the (a) *a*-direction (b) *b*-direction and (c) *c*-direction.

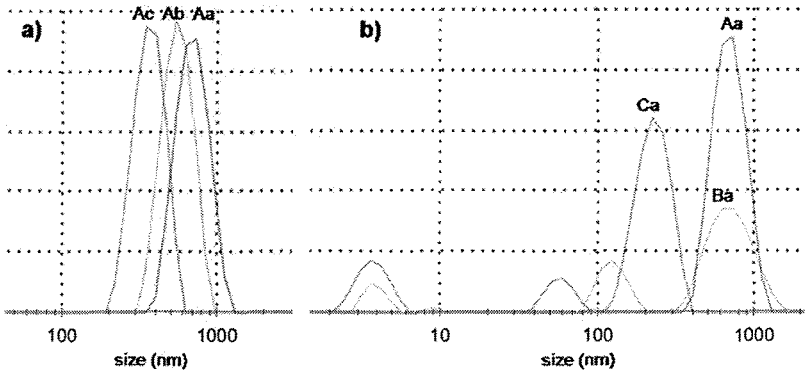

Fig. 6 Particle size distribution of intermediary species by light scattering from the solutions at 20 hours of crystallization, when (a) the Ba^{2+} concentration is 10 mM and the polymer concentration is 1.0 g L^{-1} (Aa), 0.5 g L^{-1} (Ab) or 0.1 g L^{-1} (Ac) respectively, or when (b) the polymer concentration is 1 g L^{-1} and the Ba^{2+} concentration is 10 mM (Aa), 5 mM (Ba) or 2.5 mM (Ca), respectively.

results in the largest particle size (692 nm for Aa in Fig. 6b), while several other species with smaller particle sizes were found at a lower polymer concentration.

The increase of the particle size in solution with increasing polymer concentration is against the expected trend of decreasing particle size with increasing polymer concentration due to a better colloidal stabilization of the nanoparticles. Since the particle size of the nanoparticles in solution is much bigger than the size of the primary nanoparticles in the mesocrystals (*ca.* 50–100 nm), the particles in solution detected by DLS should be aggregates. Based on this assumption, we can explain the data with the onset of "bridging aggregation", which indeed is a standard effect increasing with polymer concentration.

To reveal how the mesocrystals form, we looked at the different growth stages. At first, the polymer certainly sequesters Ba^{2+} ions, similar to Ca-ions.[32] Due to the stabilizing PEO moieties, these complexes do not precipitate, but form nanoscopic aggregates. DLS measurement shows formation of 250 nm sized aggregates when mixing only the polymer and Ba^{2+} ions at 1.0 g L^{-1} and 10 mM, respectively. Addition of CO_2 to these complexes transfers them into more compact amorphous polymer/$BaCO_3$/water intermediates with a size of 20–40 nm (TEM + SAED, data not shown), which are at the upper end of the examined polymer concentrations so stable that homogeneous nucleation can be completely suppressed. This inhibition sets in at a polymer concentration as low as 1.0 g L^{-1}.

Time dependent dynamic light scattering (DLS) on the whole investigated range of samples reveals the existence of nanoparticles in solution already at early crystallization stages. Fig. 7 shows the time dependent DLS on sample Aa ([polymer] = 1.0 g L^{-1} and [Ba^{2+}] = 10 mM). At a very early stage, *e.g.* 2 h, three species with around 4 nm, 70 nm and 420 nm were found, with the dominant species being the one with 420 nm. This size is slightly larger than that of the mixture of polymer and Ba^{2+} after addition of CO_2 (250 nm).

Increasing the crystallization time to 6 h, no obvious difference of the particle size distribution in solution was observed. When the crystallization time is 10 or 20 h, only one species was found, which is 750 nm or 690 nm,

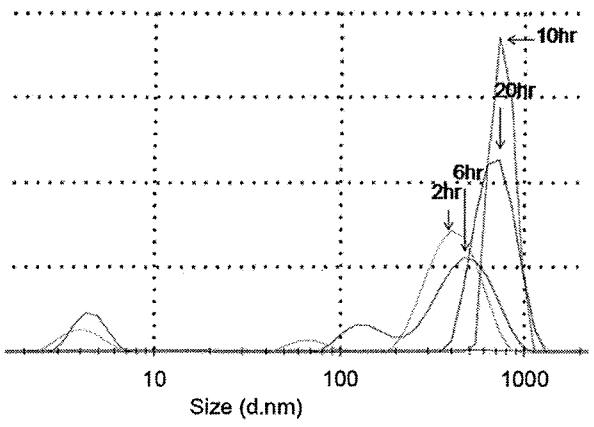

Fig. 7 Time dependent particle size distribution by light scattering from the solutions Aa ([Ba^{2+}] = 10 mM and [polymer] = 1.0 g L^{-1}).

respectively. At this time, the mesocrystals have already formed on the glass surface.

Since the initial polymer aggregates sequester Ba^{2+} ions, it is reasonable to assume that these Ba-rich aggregates also enrich the carbonate ions and thereby turn into the sites for the nucleation of amorphous $BaCO_3$ nanoparticles. The size of these nanoparticles is defined by colloidal stability and the role of the polymer additive therein. Upon particle collisions or coalescence, there are as many amorphous nanoparticles left as the system can stabilize, *i.e.* with respect to the given conditions, the system is "critically stabilized" and produces the minimal particle size possible. This size seems to be around 50–100 nm (SEM and TEM) and is remarkably monodisperse, as a result of this "primary aggregation and growth process". Polymer bridging between these particles results in slightly larger species to be followed in DLS which in addition slightly grow throughout the course of crystallization. Nevertheless, it is obvious throughout the reaction that this species is feeding and supporting the crystallization, as seen by the continuity of the time dependent data in Fig. 7.

The notation "critically stabilized" is the key for the understanding of the following steps of the process, as it means that the amorphous intermediate particles do not attract each other (as otherwise they would have aggregated), but are spontaneously attracted by any ternary body with only slightly higher Hamaker constant, say a nucleation centre at the glass surface or even another nanoparticle, which has turned in a solid state transformation into a nanocrystal. That means crystallization of the first nanoparticles (keeping about their size) also sets the start for the aggregation towards the loosely directional assembly/recrystallization process, which later generates the matured mesocrystal. This aggregation force is at the beginning admittedly weak, and the resulting aggregates are only weakly organized, but with increasing size and coupled aggregation strength, the perfection of assembly is getting higher and higher, being "feeded" by still the same colloidal solution species.

SEM investigation of mesocrystals formed at [Ba^{2+}] = 10 mM and [polymer] = 0.1 g L^{-1} also shows elliptical nanoparticle superstructures (Fig. 8). These smaller structures with sizes of 5–10 μm are found besides more developed larger dumbbell shaped mesocrystals (Fig. 8a). The early species all show the hexagonal symmetry and a large number of defects are evident due to packing imperfections and are similar to species observed by Yu *et al.* in the presence of a phosphonated block copolymer.[47] The pictures also clearly show that the structures are composed of small elongated nanoparticles (*ca.* 50–100 nm in diameter and 100–200 nm in length). It is notable that despite the defects, the overall building principle of the mesocrystal is preserved. A closer look on some mesocrystals with built in defects reveal insights into the possible building principle (Fig. 9). The early hexagonal mesocrystal species already contain the information for the following morphogenesis sequence into the dumbbell structures, which show several arms. Nevertheless, these arms are less developed than the ones for the particles shown in Fig. 3Cc which show the six + one symmetry resulting from hexagonal precursor particles.

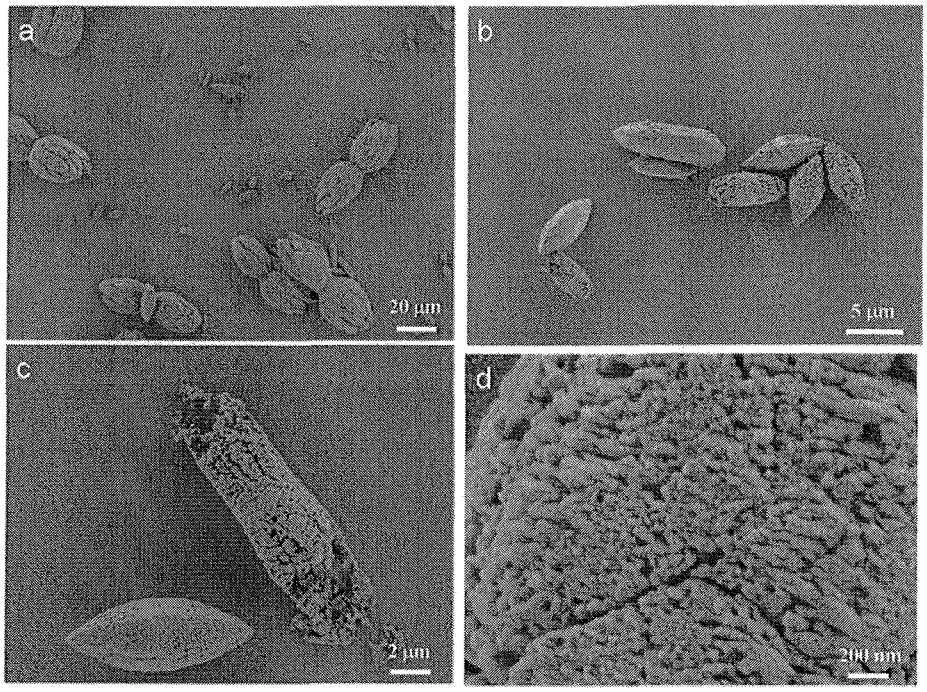

Fig. 8 Representative mesocrystal from Ac ([polymer] = 0.1 g L^{-1} and [Ba^{2+}] = 10 mM) after one week: (a) or one day: (b), (c) and (d). The defects in (b) and (c) also can be due to the effect of a dissolution process of more soluble and/or less oriented nanoparticle structures.

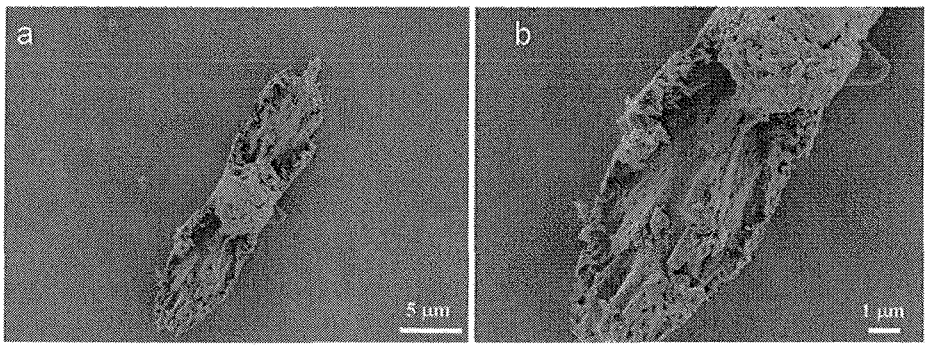

Fig. 9 SEM of defect aggregates in sample Ac. These defects can be also due to the effect of a dissolution process of more soluble and/or less oriented nanoparticle structures.

For the sample with highest Ba^{2+}-supersaturation and lowest polymer concentration (Fig. 3: Ac), the dumbbell structures are less defined. Both sides of the dumbbell are more curved, with an opening angle in the center of about 90°. The fact that this opening angle depends in a continuous fashion on Ba^{2+}-concentration speaks against controlled twinning and underlines the role of intermolecular electric splay fields as a source of long range organization, which are stronger for higher Ba^{2+}-concentrations.

The branching is still along a crude, six-fold symmetry, but some structures contain more than one ring of branches, that is the radial break-up is stronger. The defect event depicted in Fig. 10, where two superstructures were growing by coincidence very close to each other, indicates the importance of strong fields throughout particle alignment and the set-up of the superstructure. Both structures are bent towards each other,

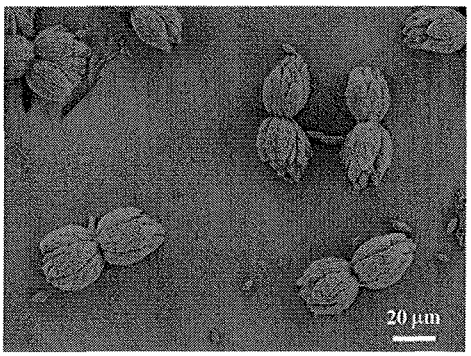

Fig. 10 Evidence for the importance of electric fields for the set-up of the nanoparticle superstructures in sample Ac ([polymer] = 0.1 g L^{-1} and [Ba^{2+}] = 10 mmol L^{-1}). Both superstructures are bent towards each other against the expectation (see text).

whereas for diffusive mass control, they would be bent away from each other (as the interior would be depleted of matter). In addition, two crystal branches are folded from the structures by attraction from the other unit, with an exact anti-parallel arrangement in the middle. This arrangement is typical for the action of electric dipole fields, while the antiparallel orientation gives a maximal compensation of the two "deviating" units.

Discussion and conclusion

The slow crystallization of barium carbonate by the gas diffusion technique in the presence of a special, ion and mineral binding PEO-*b*-polyaspartate block copolymer yielded, in dependence of varying Ba^{2+} and polymer concentrations, a family of well-defined crystalline mesostructures, *i.e.* regular scaffolds composed of well-separated, but almost perfectly 3-dimensionally aligned nanocrystals. By using HRSEM and following the development of the structures in dependence of concentration, it was possible to reveal the inner architecture principles of these mesocrystals and the role of the polymer modifier therein.

At high polymer concentration, slower heterogeneous nucleation on the walls leads to about hemispherical objects with intergrown surface spikes. HRSEM reveals that those spikes are both porous as well as composed of smaller building blocks *ca.* 20–50 nm in size. These superstructures grow by attraction of the amorphous intermediates and mesoscale transformation towards the final crystalline assemblies; classical crystallization processes are not obviously involved. As the surface reliefs are getting finer and more differentiated with lower Ba^{2+} and coupled higher polymer concentration, it is deduced that also the amorphous building units are smaller with high polymer stabilizer concentration, a reasonable and common behavior.

Lowering the polymer concentration below a critical value of about 0.5 g L^{-1}, homogeneous nucleation can set in, and a family of dumbbell-like crystal superstructures is observed. In this region, the homogeneously formed mesostructures are getting smaller with higher absolute polymer concentration. This translates into the fact that the number of seeds for mesoscale assembly is increasing with increasing polymer concentration. We therefore can clearly exclude that mesocrystal nucleation is caused by missing stabilization by the polymer; it is rather a property of the polymer stabilized nanoparticulate intermediates as such. It was speculated that nucleation of the mesostructures comes with the crystallization of individual amorphous nanoparticles, which (because of crystallization) turn colloidally unstable in an otherwise critically stabilized collective dispersion state and turn into the nucleus of a growing mesocrystal. Such nucleation events go with the concentration or even higher exponents of their concentration.

Definition and outer shape of the dumbbell structures depends also on the mineral concentration: at the lower end of polymer concentration, low Ba^{2+} concentrations lead to more organized and more facetted assembly structures, whereas higher Ba^{2+} concentrations give highly curved objects. We relate this to the speed and the inversely coupled perfection of the mesoscale assembly of the nanoparticles: the higher the intermediate concentration, the faster the growth, and the more structural defects are trapped in the structure. For the lowest polymer and lowest ion concentration of our series, *i.e.* the most "ideal" growth conditions, rather well facetted superstructures with seven crystal branches on each side of the dumbbell are observed. Polarized optical images indicate the uniform orientation of the building blocks within the dumbbell structure (Fig. S3, ESI†). HRSEM allowed us to depict the construction principles of those superstructures, which are finely textured and full of pores in the middle of the structures (and therefore at the beginning of growth), whereas the assembly is driven to more perfected structures at the 14 tips and therefore at the end of the assembly processes. This means that the structure-organizing fields are growing with the structure as such, that is the fields originate from the coherent addition of elemental fields from the primary crystalline units, mutual self-organization is a collective phenomenon.[48]

As spontaneous branching is not an inherent feature of classical crystallization processes, we attribute this to these strong dipole fields which drive nanoparticle aggregation and mesoscale transformation, and similar collective fields were already discussed[45,48] and experimentally evidenced[48] for fluoroapatite growth. Strong dipolar effects (instead of possible diffusion limitation effects) could also be evidenced by the observation of a rare defect structure where two mesocrystals sedimented in close proximity on the support and continued their growth in a coupled fashion (Fig. 10).

Although meanwhile observed in a number of cases, it is still exciting to us that such mesocrystals grown from nanocrystals can exhibit a dipolar character, whereas single crystals of the same material cannot, due to crystal symmetry reasons. We have attributed this to a dissymmetry of surface changes on the structure-constituting nanocrystals,[30] as the observed preferential growth direction (the *c*-direction of witherite) only offers the possibility of highly charged crystal splitting planes, which are stabilized by the adhering polymers.

Future work will address the importance of electric fields and electric bonding on structure formation by performing crystallization in outer electric fields or quantification of local fields, similar to the recently described fluoroapatite case.[49]

Acknowledgements

We thank the Max-Planck Society for financial support and a fellowship for T.X.W. Rona Pitschke and Heike Runge are acknowledged for the skillfully performed HRSEM investigations. Romina Sütterlin, Jessica Brand and Katharina Ostwald are acknowledged for the polymer synthesis. H.G.B. acknowledges support from the DFG Emmy Noether-Program (BO 1762/2).

References

1 H. Imai, *Biomineralization I: Crystallization and Self-Organization Process*, Topics in Current Chemistry, ed. K. Naka, Springer, New York, 2007, vol. 270, p. 43.
2 F. C. Meldrum and H. Cölfen, *Chem. Rev.*, 2008, **108**, 4332.
3 M. Lahav and L. Leiserowitz, *Chem. Eng. Sci.*, 2001, **56**, 2245.

4 L. A. Estroff and A. D. Hamilton, *Chem. Mater.*, 2001, **13**, 3227.
5 H. Cölfen and S. Mann, *Angew. Chem., Int. Ed.*, 2003, **42**, 2350.
6 S. H. Yu and H. Cölfen, *J. Mater. Chem.*, 2004, **14**, 2124.
7 H. Cölfen and S. H. Yu, *MRS Bull.*, 2005, **30**, 727.
8 S. A. Davis, M. Breulmann, K. H. Rhodes, B. Zhang and S. Mann, *Chem. Mater.*, 2001, **13**, 3218.
9 H. Cölfen and M. Antonietti, *Angew. Chem., Int. Ed.*, 2005, **44**, 5576.
10 M. Cusack and A. Freer, *Chem. Rev.*, 2008, **108**, 4433.
11 M. B. Dickerson, K. H. Sandhage and R. R. Naik, *Chem. Rev.*, 2008, **108**, 4935.
12 L. B. Gower, *Chem. Rev.*, 2008, **108**, 4551.
13 N. A. J. M. Sommerdijk and G. de With, *Chem. Rev.*, 2008, **108**, 4499.
14 J. L. Arias and M. S. Fernndez, *Chem. Rev.*, 2008, **108**, 4475.
15 A. George and A. Veis, *Chem. Rev.*, 2008, **108**, 4670.
16 M. Hildebrand, *Chem. Rev.*, 2008, **108**, 4855.
17 L. J. Wang and G. H. Nancollas, *Chem. Rev.*, 2008, **108**, 4628.
18 R. Q. Song and H. Colfen, *Adv. Mater.*, 2010, **22**, 1301.
19 M. Niederberger and H. Cölfen, *Phys. Chem. Chem. Phys.*, 2006, **8**, 3271.
20 H. Cölfen and M. Antonietti, *Mesocrystals and Non Classical Crystallization*, John Wiley & Sons, Chichester, 2008.
21 L. Zhou and P. O'Brien, *Small*, 2008, **4**, 1566.
22 E. Matijevic and P. Sheiner, *J. Colloid Interface Sci.*, 1978, **63**, 509.
23 W. P. Hsu, L. Ronnquist and E. Matijevic, *Langmuir*, 1988, **4**, 31.
24 S. H. Lee, Y. S. Her and E. Matijevic, *J. Colloid Interface Sci.*, 1997, **186**, 193.
25 B. Judat and M. Kind, *J. Colloid Interface Sci.*, 2004, **269**, 341.
26 Y. R. Ma, H. Cölfen and M. Antonietti, *J. Phys. Chem. B*, 2006, **110**, 10822.
27 Y. Oaki, A. Kotachi, T. Miura and H. Imai, *Adv. Funct. Mater.*, 2006, **16**, 1633.
28 D. Vielzeuf, N. Floquet, D. Chatain, F. Bonnete, D. Ferry, J. Garrabou and E. M. Stolper, *Am. Mineral.*, 1995, **2–3**, 242.
29 T. X. Wang, H. Cölfen and M. Antonietti, *J. Am. Chem. Soc.*, 2005, **127**, 3246.
30 T. X. Wang, M. Antonietti and H. Cölfen, *Chem.–Eur. J.*, 2006, **12**, 5722.
31 T. X. Wang, A. Verch, H. Börner, H. Cölfen and M. Antonietti, *J. Ceram. Soc. Jpn.*, 2009, **117**, 221.
32 D. Gebauer, H. Cölfen and A. Verch, *Adv. Mater.*, 2009, **21**, 435.
33 H. Cölfen and L. M. Qi, *Chem.–Eur. J.*, 2001, **7**, 106.
34 Y. R. Ma, H. Cölfen and M. Antonietti, *J. Phys. Chem. B*, 2006, **110**, 10822.
35 G. Wulff, *Z. Kristallogr.*, 1901, **34**, 449.
36 R. Agra, F. van Wijland and E. Trizac, *Phys. Rev. Lett.*, 2004, **93**, 018304.
37 J. F. Lutz and H. G. Börner, *Prog. Polym. Sci.*, 2008, **33**, 1.
38 D. Eckhardt, M. Groenewolt, E. Krause and H. G. Börner, *Chem. Commun.*, 2005, 2814.
39 J. Hentschel, E. Krause and H. G. Börner, *J. Am. Chem. Soc.*, 2006, **128**, 7722.
40 S. Albeck, S. Weiner and L. Addadi, *Chem.–Eur. J.*, 1996, **2**, 278.
41 G. Wegner, P. Baum, M. Mullert, J. Norwig and K. Landfester, *Macromol. Symp.*, 2001, **175**, 349.
42 M. G. Page, N. Nassif, H. G. Börner, M. Antonietti and H. Cölfen, *Cryst. Growth Des.*, 2008, **8**, 1792.
43 P. Simon, E. Rosseeva and J. Buder, *Adv. Funct. Mater.*, 2009, **19**, 3596.
44 R. Kniep and S. Busch, *Angew. Chem., Int. Ed. Engl.*, 1996, **35**, 2624.
45 S. Busch, H. Dolhaine, A. DuChesne, S. Heinz, O. Hochrein, F. Laeri, O. Podebrad, U. Vietze, T. Weiland and R. Kniep, *Eur. J. Inorg. Chem.*, 1999, 1643.
46 S. Busch, U. Schwarz and R. Kniep, *Adv. Funct. Mater.*, 2003, **13**, 189.
47 S. H. Yu, H. Cölfen and M. Antonietti, *J. Phys. Chem. B*, 2003, **107**, 7396.
48 R. Paparcone, R. Kniep and J. Brickmann, *Phys. Chem. Chem. Phys.*, 2009, **11**, 2186.
49 P. Simon, D. Zahn, H. Lichte and R. Kniep, *Angew. Chem., Int. Ed.*, 2006, **45**, 1911.